Batteries

Multifunctional Self-Assembled Bio-Interfacial Layers for High-Performance Zinc Metal Anodes

Jiahui Lu, Tianyi Wang,* Jian Yang, Xin Shen, Huan Pang, Bing Sun,* Guoxiu Wang,* and Chengyin Wang*

Abstract: Rechargeable aqueous zinc-ion (Zn-ion) batteries are widely regarded as important candidates for next-generation energy storage systems for low-cost renewable energy storage. However, the development of Zn-ion batteries is currently facing significant challenges due to uncontrollable Zn dendrite growth and severe parasitic reactions on Zn metal anodes. Herein, we report an effective strategy to improve the performance of aqueous Zn-ion batteries by leveraging the self-assembly of bovine serum albumin (BSA) into a bilayer configuration on Zn metal anodes. BSA's hydrophilic and hydrophobic fragments form unique and intelligent ion channels, which regulate the migration of Zn ions and facilitate their desolvation process, significantly diminishing parasitic reactions on Zn anodes and leading to a uniform Zn deposition along the Zn (002) plane. Notably, the Zn||Zn symmetric cell with BSA as the electrolyte additive demonstrated a stable cycling performance for up to 2400 hours at a high current density of 10 mA cm^{-2}. This work demonstrates the pivotal role of self-assembled protein bilayer structures in improving the durability of Zn anodes in aqueous Zn-ion batteries.

[*] J. Lu, Prof. T. Wang, X. Shen, Prof. H. Pang, Prof. C. Wang
School of Chemistry and Chemical Engineering
Yangzhou University
225002 Yangzhou, Jiangsu Province, P. R. China
E-mail: wangty@yzu.edu.cn
        wangcy@yzu.edu.cn

Dr. B. Sun, Prof. G. Wang
Centre for Clean Energy Technology
School of Mathematical and Physical Science
Faculty of Science
University of Technology Sydney
2007 Broadway, NSW, Australia
E-mail: bing.sun@uts.edu.au
        guoxiu.wang@uts.edu.au

J. Yang
Key Lab of Fluorine and Silicon for Energy Materials and Chemistry
of Ministry of Education
College of Chemistry and Chemical Engineering
Jiangxi Normal University
330022 Nanchang, Jiangxi Province, P. R. China

Introduction

Aqueous Zinc-ion (Zn-ion) batteries have attracted significant attention recently as viable alternatives for energy storage systems.[1] Distinct from conventional lithium and sodium-based rechargeable batteries, Zn-ion batteries employ non-toxic aqueous electrolytes and abundant Zn metal, highlighting their advantages in safety, environmental protection, and sustainability for grid-scale applications.[2] In addition, the Zn metal anode has a high theoretical capacity of 820 mAh g^{-1} and a relatively low electrode potential (-0.76 V *vs.* standard hydrogen electrode).[3] However, despite the above-mentioned advanced characteristics, the widespread implementation of Zn-ion batteries is facing significant challenges, most of which are related to the poor electrochemical performance of Zn metal anodes.[4] The first issue is the formation of dendrites during repeated Zn plating/stripping processes, leading to short circuits and failure of batteries.[5] Meanwhile, the Zn anode is susceptible to corrosion and generates byproducts (e.g., $Zn_4SO_4(OH)_6 \cdot xH_2O$).[6] These inactive byproducts accumulate on the surface of the Zn anode and obstruct Zn^{2+} ion transfer, severely intensifying surficial passivation and reducing the battery's cycling stability.[7]

Several strategies have been proposed to remedy the inherent issues of Zn metal anodes. These include optimizing electrolyte composition, enhancing separator structure, and creating a durable electrode/electrolyte interface.[8] Among them, constructing an artificial solid electrolyte interphase (SEI) layer by an ex situ or in situ method to inhibit the growth of Zn dendrites and suppress parasitic reactions has been regarded as the most effective strategy.[8a,9] Ex situ methods involve pre-immobilizing a high ionic conductive layer to enhance Zn^{2+} ion diffusion, reduce surface passivation, and prevent dendritic growth.[10] However, the ex situ-formed SEI layer bears the risk of exfoliating from the Zn substrate after multiple cycles, which may deteriorate at high current densities. Conversely, the in situ method spontaneously forms an SEI layer through chemical reactions, self-assembly or polymerization from electrolyte additives, which can improve the dynamic stability of the Zn metal anode by maintaining the integrity of the Zn metal anode under real-time protection.[11] For instance, introducing $Zn(H_2PO_4)_2$ into the aqueous electrolyte led to the formation of a compact $Zn_3(PO_4)_2 \cdot 4H_2O$ SEI layer, promoting uniform Zn^{2+} ion flux and preventing dendrite formation.[12] Similarly, a trace amount of hexamethylenetetramine (HMTA) in the aqueous electro-

lyte in situ forms an anode–molecule interface on the Zn anode, inhibiting the hydrogen evolution reaction and enhancing the interfacial stability.[13] Nonetheless, cost and environmental friendliness are still non-negligible issues that must be considered. Therefore, some biological macromolecules, usually represented by proteins, have demonstrated promising potential as multifunctional electrolyte additives to form interfacial protective layers.[14] Their unique amphiphilic properties and complex molecular structure endow proteins with rich biochemical characteristics to facilitate metal ion diffusion, not to mention their inherent environmentally benign and biodegradable properties.[15] For example, poly-l-glutamic acid (PGA) was employed as a multifunctional electrolyte additive to construct a dynamic adsorption layer on the Zn anode, which effectively suppressed hydrogen evolution by decreasing the activity of H_2O molecules.[16] Furthermore, incorporating serine in the aqueous electrolyte has proven its ability to induce the deposition of Zn along the favorable Zn (002) plane rather than the Zn (100) plane, thereby mitigating dendrite growth.[17] Therefore, employing environmentally benign and biodegradable biological macromolecules as multifunctional electrolyte additives represents a promising and sustainable strategy to enhance the electrochemical performance of Zn-ion batteries.

Herein, we employ bovine serum albumin (BSA), a classic carrier protein with a self-assembly feature in aqueous solutions, as an electrolyte additive to construct a multifunctional interfacial layer on the Zn metal anode. By folding hydrophilic/hydrophobic chains, the BSA molecules can self-assemble on the surface of the Zn metal anode and form a dynamic multifunctional bilayer with a unique anti-solvation effect, which promotes the desolvation process of solvated Zn^{2+} ions. The inherent ion diffusion channels of BSA facilitate homogeneous Zn^{2+} ion diffusion to the Zn metal anode while blocking the free water molecules and SO_4^{2-} anions. As a result, incorporating a BSA bilayer on the Zn anode remarkably improved the cycling stability of Zn||Zn symmetric cells, achieving 2400 hours of stable cycling performance. Concurrently, the Zn||V_2O_5 full cell demonstrates a high-capacity retention of 94.69% for 4800 cycles at 5 A g^{-1}.

Results and Discussion

The BSA consists of 607 amino acid residues.[18] Compared with other conventional proteins, the unique molecular structure of BSA endows it to chelate with Zn^{2+} ions and form Zn ion diffusion channels (Figure S1).[19] Figure 1a elucidates the formation of the BSA-based protective layer on the Zn metal anode via self-assembling processes. The participation of BSA molecules can significantly change the surface structure of the Zn metal anode from an electrical double layer to a multifunctional BSA bilayer (Figures 1a and 1b). When dissolved in the ZnSO$_4$ electrolyte, BSA molecules can assemble into micelles with hydrophilic chains facing outward and hydrophobic chains facing inwards. Because the pH value of the aqueous ZnSO$_4$ electrolyte

(~4.3) is lower than the isoelectric point of BSA (~4.7), BSA micelles are positively charged. They can spontaneously migrate toward the Zn metal anode under the driving force of the electric field.[20] With the accumulation of the BSA micelles on the surface of the Zn anodes, those micelles would merge and assemble into a multifunctional interfacial layer with a hydrophilic-hydrophobic-hydrophilic sandwich-like structure (Figure 1c). As a typical carrier protein, the BSA bilayer can enhance the interface Zn affinity by chelating with Zn^{2+} ions and constructing an ionic channel to promote uniform Zn^{2+} ion flux and facilitate their uniform deposition. In addition, solvent molecules (e.g., free water molecules and solvated water molecules in $[Zn(H_2O)_6]^{2+}$) are blocked by the internal hydrophobic layer, thereby reducing the occurrence of side reactions.

To confirm the above hypothesis, we first employed cryogenic electron microscopy (Cryo-EM) to characterize the BSA micelles in the ZnSO$_4$ electrolyte. As shown in Figure 1d, with 0.5 wt% BSA as the additive, most BSA molecules disperse uniformly in the electrolyte as micelles with a diameter of 10–40 nm, which is consistent with the particle size distribution in Figure S2. The zeta potential testing results confirm that BSA micelles are positively charged in the aqueous electrolyte (Table S1). In addition, the electrolyte with the BSA additive exhibited an obvious Tyndall effect (Figure S3). The contact-angle tests showed that the presence of the BSA bilayer significantly improved the wettability of the Zn anode in the aqueous electrolyte (Figure S4). The protein electrophoresis test was carried out using the polyacrylamide gel electrophoresis method and the results are shown in Figure 1e and S5. The Native Poly-acrylamide Gel Electrophoresis (Native-PAGE) testing results successfully captured the migration trajectory of BSA molecules towards the Zn anode driven by the electric field (marked by bromothymol blue). This marks the first direct visualization of the movement of protein molecules in a battery electrolyte. In addition, the small-angle X-ray scattering (SAXS) and Brunauer–Emmett–Teller (BET) test results confirm that the BSA layer exhibits typical pore size distribution and structural characteristics of ion channels (Figure S6 and S7).

The fluorescence luminescence method was employed to investigate the distribution of the BSA layer around defects of the Zn anode.[21] As shown in Figure 1f, a piece of Zn metal anode with a pre-drilled pinhole was retrieved from an electrolyte containing 5 wt% dyed BSA. After being washed with deionized water and radiated under ultraviolet (UV) light, the fluorescence intensities from the edges and sharp tips are much stronger than those in the other flat areas. This phenomenon demonstrates that BSA can spontaneously adhere to areas with large curvature (such as Zn buds and defects) even in aqueous electrolytes due to positive synergistic effects. Owing to the much lower electronic conductivity of BSA compared to Zn metal, the distribution of the surrounding electric field is altered, hence changing the depositing orientation of subsequent Zn^{2+} ions. Especially, the neighborhood BSA molecules attract each other through intermolecular hydrogen bonding or van der Waals forces, which means that the multifunctional BSA
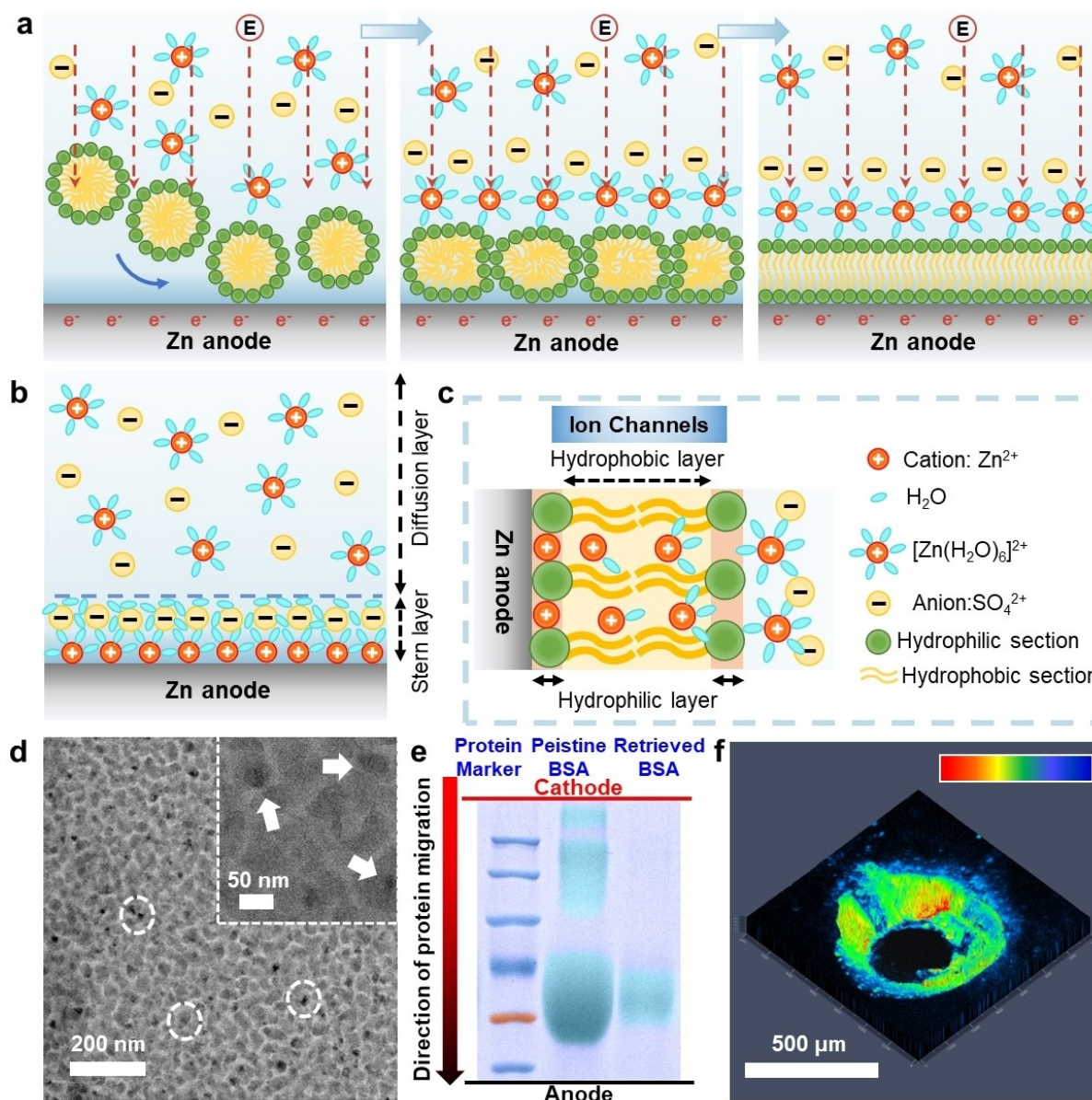
Figure 1. a) Illustration for the formation of the BSA bilayer on the Zn anode. b) Schematic diagram of the electrical double layer of a Zn metal anode. c) Cross-sectional schematic diagram of multifunctional BSA bilayer and the corresponding working mechanism of Zn^{2+} ion diffusion. d) Cryo-EM image of BSA micelles dispersed in the aqueous electrolyte. The insert is the corresponding high-magnified snapshot. e) Native-PAGE result displays the migration trace of pristine BSA and BSA retrieved from the electrolyte. f) The 2.5-dimensional fluorescent image of BSA distribution around the edge and protrusions on a Zn metal foil under UV light. The scale bars on the top correspond to the intensity increase from blue to red.

bilayer has extremely high fluidity and can be extended or stretched with the expansion of the Zn deposition layer by accepting new BSA micelles.

Previous research confirmed that protein molecules cannot exist stably under high-energy electron beams, which is challenging to observe non-destructively.[22] Hence, we employed the Cryo-EM and the thin film vitrification (TFV) method to quickly preserve the protein bilayer immobilized on the Zn surface in aqueous electrolyte at a "wet" status.[23] The sample preparation process for the Cryo-EM investigation via the TFV method is presented in Figure S8. As

shown in Figure S9a–b, the Zn deposited in the pristine electrolyte exhibits numerous fresh buds on the surface of typical hexagonal dendrites. According to the previous report, these buds are nucleation sites that induce the growth of Zn dendrites.[24] Conversely, the Zn deposited in the BSA-added electrolyte demonstrates a smooth and fluent interface (Figure 2a and Figure S9c). In addition, a polymetric layer with an average thickness of 80 nm consisting of two separated BSA layers can be identified with a boundary line. Furthermore, according to the Energy Dispersive X-ray Spectroscopy (EDS) results (Figure S10),
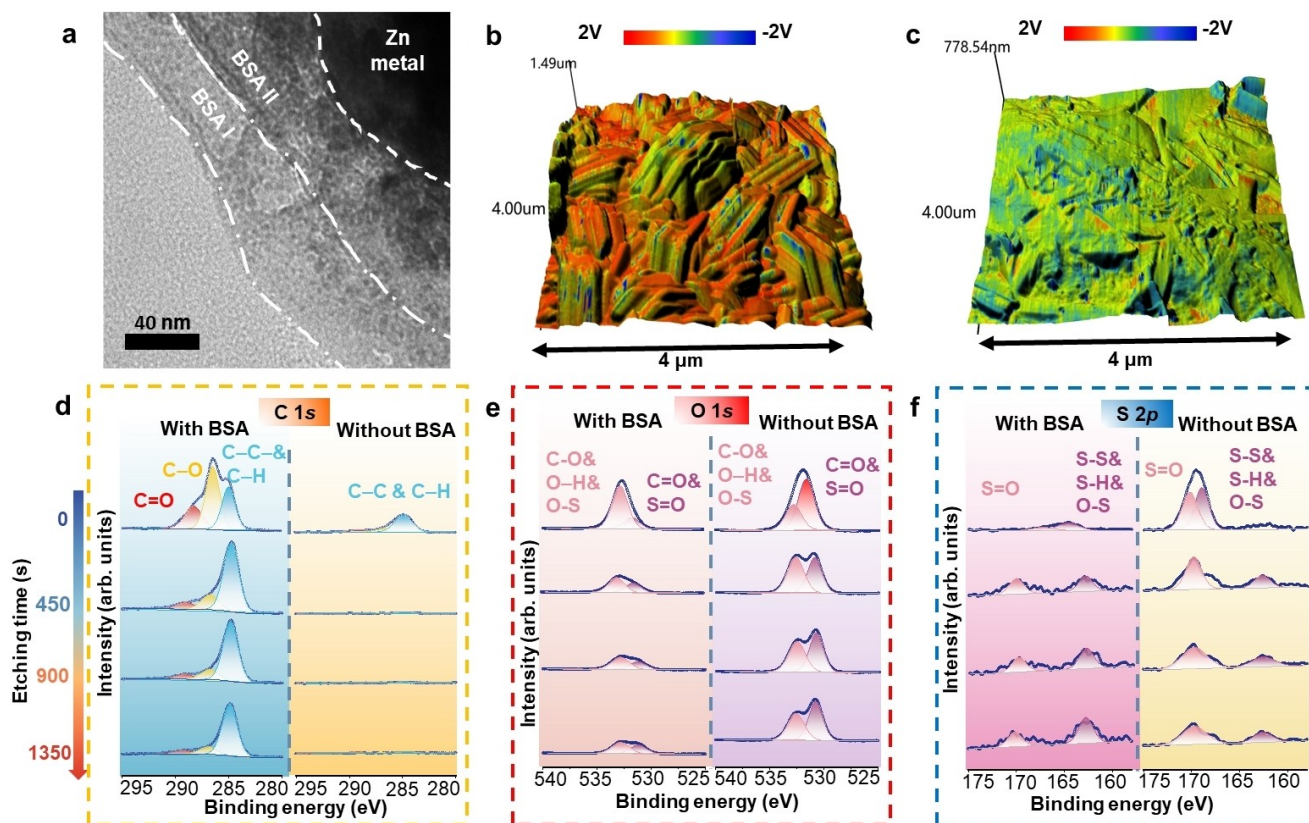
Figure 2. a) The Cryo-EM image of the BSA bilayer formed on the Zn deposits. b), c) Surface morphology and corresponding potential distribution mapping of Zn deposition layers characterized by KPFM in the electrolyte without (b) and with BSA additives (c). d)–f) XPS depth profiling of SEI formed in aqueous electrolytes with and without BSA. d) C 1s, e) O 1s and f) S 2p spectra.

there is a noticeable difference in the presence of sulphur on the Zn deposition obtained in the electrolyte with BSA compared to the electrolyte without BSA, indicating the inclusion of BSA changes the elemental composition of the SEI layer of the Zn anode. To investigate the stability of the BSA-based SEI layer during extended cycling, X-ray photoelectron spectroscopy (XPS) analysis was conducted on Zn anodes retrieved from Zn∥Zn symmetric cells with and without BSA additive in the electrolytes after 200 cycles. By comparing the XPS spectra of the cycle Zn anodes (Figure S11) with the XPS spectra of the pristine BSA powder (Figure S15), we confirmed that the SEI on the anode surface contains components derived from BSA, indicating that the BSA-induced SEI remains intact and stable after long-term cycles. In addition, two-photon confocal microscopy analysis confirmed that the BSA-induced SEI layer shows enhanced stability by forming a uniform and resilient protective coating layer on the Zn metal surface. This layer effectively mitigates dendrite formation and corrosion, maintaining a smoother and more stable SEI during cycling (Figure S12).

The high-resolution Kelvin probe force microscopy (KPFM) was used to map the variations of the local electric properties of Zn deposition layers in the aqueous electrolyte with and without BSA additive. Additional images and

detailed data for KPFM can be found in Figure S13. Figure 2b shows that the Zn deposition layer in the pristine electrolyte exhibits a height fluctuation ranging up to 1.49 μm. This deposition morphology illustrates the prominent vertical Zn dendrites with a significantly uneven distribution of surface potentials. High potentials are concentrated at the edge of the dendrites, where the potential intensities increase from blue to red, indicating a significant variation in surface potential. Conversely, as shown in Figure 2c, with the addition of BSA in the electrolyte, the Zn deposit exhibits a smoother and more uniformly distributed layer with significantly reduced height fluctuations (~0.77 μm). The surface of the Zn deposition layer with the BSA additive appeared electrically neutral without extremely concentrated potentials. The changes in the distribution of electric field intensities mainly stem from the higher dielectric constant of proteins flattening the polarization range of the electric field.

The chemical composition of the SEI formed on the Zn metal anodes in the electrolytes with and without the BSA additive was analyzed by XPS depth profiling analysis. The full survey spectra analysis in Figure S14 revealed that the SEI formed on the Zn deposition with the BSA additive yielded increased C and N contents, and reduced O and S contents compared to the SEI formed in the pristine

electrolyte. Before etching, all elemental spectra of SEI formed in the aqueous electrolyte with BSA additive are similar to the spectra of the original BSA protein (Figure S15), confirming the presence of absorbed BSA additive. With the increased etching time, the C and N content of the Zn layer deposited with the BSA rapidly decreases. In particular, the signal representing C=O, C–O in the C $1s$ spectrum decreases significantly (Figure 2d).[25] In addition, the difference between the O $1s$ and S $2p$ spectrum also proved that the presence of the BSA bilayer could significantly reduce the side reactions between the Zn metal anodes and the $ZnSO_4$ electrolyte. As depicted in Figure 2e, in the O $1s$ spectrum of Zn deposited in the pristine electrolyte, a prominent peak corresponding to ZnO has been observed (located at 531.6 eV), which is absent in the spectrum of the sample deposited with BSA additive.[26] This observed phenomenon can be attributed to the sample's inherent susceptibility to oxidation upon exposure to the atmosphere during drying, leading to the formation of a trace amount of oxide.

Crucially, the presence of the BSA bilayer acts as a protective layer, which effectively stabilizes the Zn anode against oxidation. In Figure 2f, the clear contrast of S $2p$ signal intensity between the two samples verifies that the BSA bilayer can effectively reduce the generation of by-products (e.g., $Zn_4SO_4(OH)_6 \cdot xH_2O$). Compared with the sample obtained without BSA, in which the S=O peak dominates in the spectrum, the proportion of the peaks representing S–S bonds dominates in the spectra at all stages for the sample obtained with BSA, mainly due to the presence of BSA molecules.[27] These features confirm that the BSA bilayer can generate high affinity with the Zn metal anodes. Furthermore, the sample with BSA additives exhibits earlier Cu signals during the etching process (Figure S16a). This phenomenon indicates that the existence of a BSA bilayer can effectively reduce the generation of 'Dead Zn', which has been considered as the culprit causing the capacity decay of Zn-ion batteries.[28]

We assembled Zn||Zn transparent cells to observe the Zn deposition behaviors in different electrolytes. As shown in Figure 3a, in the initial stage, burr-like Zn buds appear on the Zn foil in the pristine electrolyte. The surface of the Zn electrode is gradually covered by scaly hexagonal Zn flakes after 12 minutes. Shortly after that, Zn dendrites appeared on top of the Zn deposit, which could result in the formation of 'Dead Zn' in the following stripping process.[29] In contrast, in the electrolyte with BSA, a uniform and compact Zn deposition layer without dendrites was observed under the same deposition condition. We then employed scanning electron microscopy (SEM) to observe the morphologies of Zn deposits. As shown in Figure 3b, the surface of the cycled Zn anode in the pristine electrolyte exhibited a rough texture with agglomerated Zn flakes, most of which were oriented vertically. The uncontrolled growth of such vertical dendrites is believed to be the main cause of 'Dead Zn' and potential internal short circuits.[30] In contrast, a smooth and compact deposition layer is observed on the Zn metal anode after cycling in the electrolyte with BSA (Figure 3d). The significant differences in the cross-sectional SEM images highlight the variations in deposition behaviors (Figure 3c and 3e).[31] The addition of BSA plays a critical role in modulating the size and morphology of the Zn deposits. The SEM images of cycled electrodes provide direct evidence to support this effect, as depicted in Figure S17. These results further validate the pivotal role of BSA in controlling the surface morphology of the Zn metal anodes during the extended stripping/plating processes.

The crystal structure of Zn deposition layers after cycling was examined using X-ray diffraction (XRD) analysis. After 200 cycles, the Zn anodes cycled in the pristine electrolyte displayed significant impurity peaks, corresponding to $Zn_4SO_4(OH)_6 \cdot xH_2O$ (Figure 3f).[9a] In contrast, there are no obvious impurity peaks in the XRD patterns of the Zn anodes cycled in the electrolyte with BSA. Due to the unique hexagonal-close packed (HCP) structure of Zn metal, the Zn (002) plane has a smoother atomic arrangement, higher atomic density, and lower surface energy than other crystal planes (e.g., (101) and (100) planes), resulting in a uniform interface charge density and tight atomic bonding.[32] Therefore, the $I_{(002)}/I_{(100)}$ ratio is regarded as an essential indicator for uniform Zn deposition. For the Zn anodes cycled in the pristine electrolyte, the $I_{(002)}/I_{(100)}$ ratio decreased from 2.01 to 1.75 after 200 cycles, favoring the formation of the (100) plane (Figure 3g). On the other hand, the Zn anodes cycled in BSA-containing electrolyte showed an increase in the $I_{(002)}/I_{(100)}$ ratio (1.99 to 2.10), suggesting more horizontal Zn deposition along the Zn (002) plane.

The solvation structure of Zn^{2+} ions in the aqueous electrolyte significantly influences the desolvation and deposition processes, and introducing additives in the electrolyte can influence the Zn^{2+} solvation structure.[33] Ab initio molecular dynamic (AIMD) simulations were used to probe Zn^{2+} solvation structures in the aqueous electrolyte with and without BSA additives. BSA contains multiple cysteine residues, which are vital for its structural integrity and biochemical features due to their ability to form disulfide bonds (S–S).[34] The S–S bonds of cysteine are particularly reactive, making it a representative unit for studying solvation dynamics. Therefore, the cysteine unit was chosen for the AIMD simulation due to its significant presence in BSA, which was confirmed by Fourier transform infrared spectroscopy (FTIR) analysis (Figure S18).[35] As shown in Figures 4a and 4b, BSA molecules can replace H_2O molecules in the Zn^{2+} ion solvation structure to reduce the number and activity of H_2O molecules near the surface of the Zn anode during the Zn deposition process. Radial distribution functions (RDFs) of Zn–S and Zn–O pairs were further studied to analyze the impact of BSA on Zn^{2+} solvation structure. As compared in Figure 4c, BSA molecules dominate the first solvation shell of Zn^{2+}, as identified by the peaks of Zn–S (BSA) and Zn–O (BSA) bond at 2.03 Å and 2.39 Å, respectively. Conversely, in the absence of BSA, H_2O molecules occupy from the first to the outermost solvation shells, where Zn–O (H_2O) interaction is measured at 2.39 Å and 3.01 Å (Figure 4d). The AIMD simulations confirm that BSA displaces water molecules in the solvation shell of Zn^{2+} ions and substantially weakens their coordination interactions. The solvation of a single
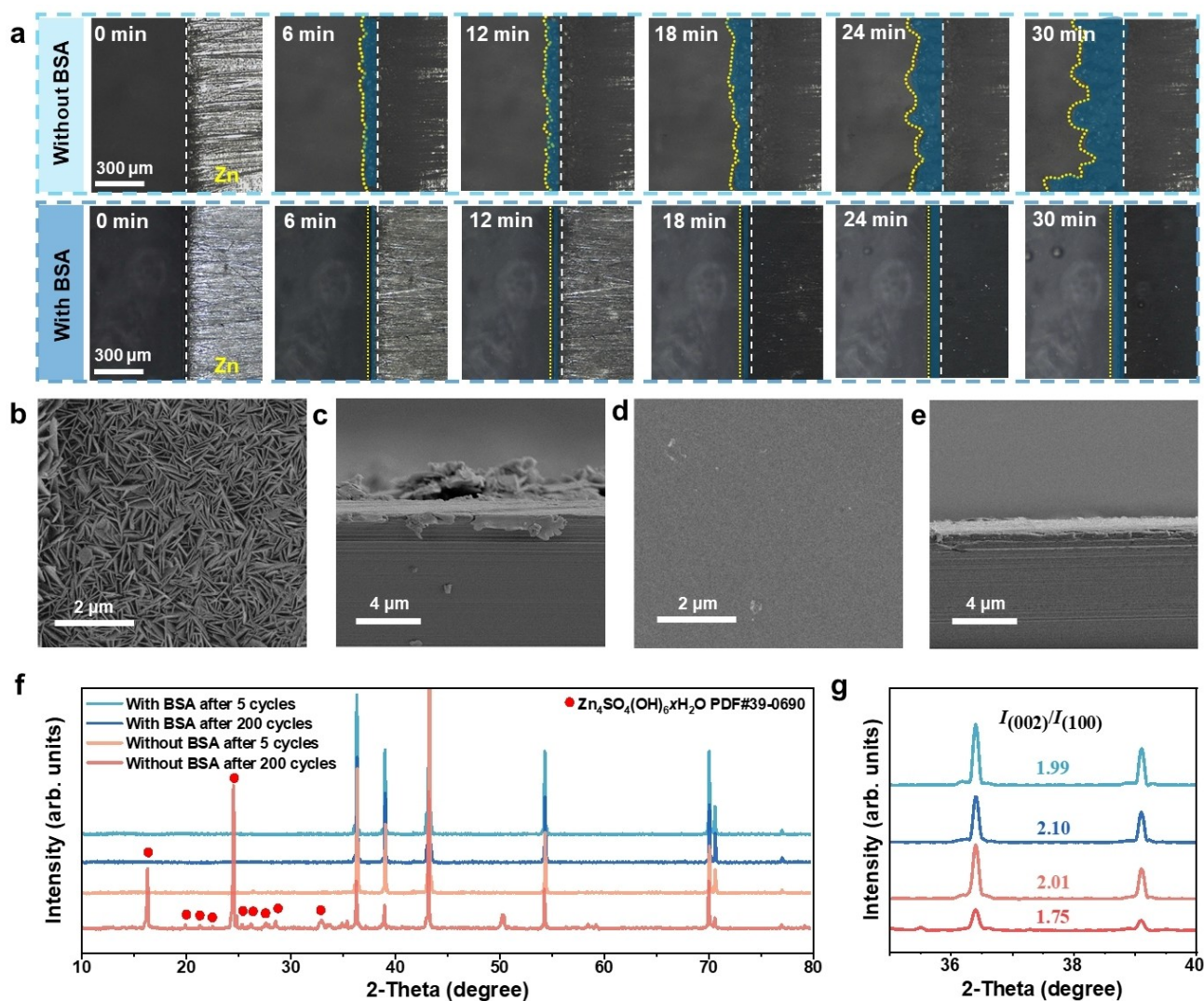
Figure 3. a) In situ observations of Zn deposition in the transparent glass cell with different electrolytes at a current density of 5 mA cm^{-2}. b), d) Top-view and c), e) cross-sectional SEM images of the Zn anode obtained (b, c) in pristine electrolyte and (d, e) in the electrolyte with BSA after depositing at 1 mA cm^{-2} for 5 h. f), g) XRD patterns of Zn anodes retrieved from Zn||Zn symmetric cells with and without BSA after cycling.

shell is of lesser magnitude than that of a double shell, facilitating faster mobility within the electrolyte and expediting the desolvation of Zn^{2+} at the electrode interface.[36] Compared to Zn^{2+} ion solvation with H_2O, Zn^{2+} solvation with BSA results in a smaller solvation shell, reducing BSA spatial repulsion at the SEI and enhancing Zn^{2+} reaction dynamics.

By calculating the specific solvation energy (E_s) and desolvation energy ($E_{des,x}$) of BSA and H_2O in Zn^{2+} complexes (Figure S19), we unveiled the Zn^{2+} desolvation process with BSA and H_2O. The solvation energy to form $[Zn–H_2O]^{2+}$ and $[Zn–(H_2O)_2]^{2+}$ structures in $ZnSO_4$ electrolyte are -0.1333 eV and -0.2455 eV, respectively (Figure 4e). Upon adding BSA, the solvation energy required to form $[Zn–BSA]^{2+}$ and $[Zn–BSA_2]^{2+}$ structures decrease significantly to -0.35915 eV and -1.0507 eV, respectively. The reduction in solvation energy facilitates more favorable conditions for the rapid and reversible insertion and

extraction of Zn^{2+} ions through the SEI.[37] The significant alterations in the Zeta potential of BSA (Table S1) verify that chelating with Zn^{2+} ions can largely improve the positive potential of BSA molecules, thereby compensating for the decrease in mobility caused by their spatial hindrance. This pre-bonding strategy also promotes the formation of ion channels in the BSA bilayer, effectively enhancing the surficial Zn^{2+} affinity during consequent deposition.[38]

Among the three principal crystal planes of Zn metal, the Zn (101) and Zn (100) planes exhibit uneven atomic arrangements and interface charge distributions, which increase the risk of dendritic growth.[39] In contrast, the Zn (002) plane is characterized by a smooth atomic arrangement and high atomic density, which results in low surface energy.[40] This configuration facilitates the parallel deposition of Zn^{2+} ions to the anode, effectively inhibiting the growth of dendrites at the Zn anode and enhancing its
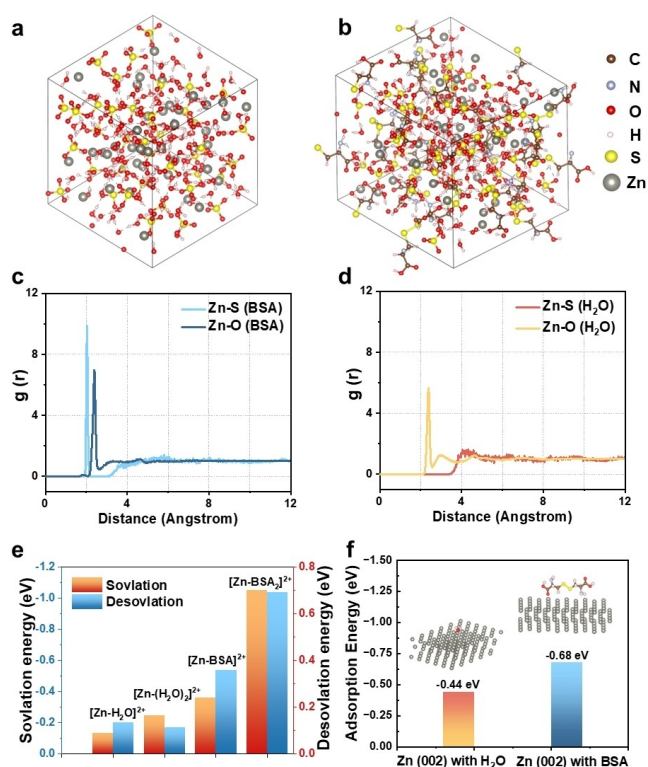
Figure 4. a), b) The AIMD simulation snapshots of the solvation structures of Zn^{2+} ions in the electrolytes (a) without and (b) with BSA. c), d) RDFs g(r) of Zn–S and Zn–O pairs (c) with BSA and (d) with H_2O. e) Solvation energy and desolvation energy of Zn^{2+} with H_2O and BSA molecules. f) Comparison of adsorption energies of BSA and H_2O toward Zn (002) plane.

corrosion resistance.[41] Herein, our calculation focused on the Zn (002) plane to evaluate the influence of BSA in modulating its properties. The adsorption energy (E_{ads}) between H_2O and BSA with Zn (002) plane is calculated using the following equation:[15b,42]

$$E_{ads} = E_{BSA/H_2O+Zn(002)} - \left(E_{BSA/H_2O} + E_{Zn(002)}\right)$$

The charge difference and adsorption energy of the Zn (002) plane with H_2O and BSA are presented in Figure S20. Notably, the charge difference distribution of the Zn (002) plane with H_2O is more localized than that with BSA. Furthermore, the adsorption energy of the Zn (002) plane with BSA (-0.68 eV) is higher than that with H_2O (-0.44 eV) (Figure 4f). Based on the density functional theory (DFT) calculations, it has been observed that BSA has a greater tendency to adsorb on the Zn (002) plane than H_2O. This is due to the strong interactions between the functional groups of carboxyl and amide, which helps reduce the interaction between Zn and H_2O, thereby minimizing side reactions.[37b,43]

We employed linear sweep voltammetry (LSV) to test the electrochemical stability windows (ESW) of Zn metal anodes with and without BSA. As shown in Figure 5a, the BSA bilayer can effectively extend the ESW from -0.75 V– 1.53 V to -0.76 V–1.57 V at a scanning rate of 0.1 mV S^{-1},

confirming its improved resistance to water decomposition.[44] The addition of BSA shifted the corrosion potential of the Zn metal anode from -0.82 V to -0.80 V (*vs.* Ag/AgCl electrode) (Figure 5b). The reduction in corrosion potential and the expansion of the ESW suggest that the internal hydrophobic layer of the BSA bilayer effectively diminishes the involvement of water molecules in electrochemical reactions on the Zn metal surface, thereby mitigating corrosion induced by hydrogen evolution. Figure 5c shows the electrochemical impedance spectroscopy (EIS) measurement results on Zn∥Zn symmetric cells at different cycles. The EIS plots indicate that during the cycling process, the impedances of the batteries showed a gradually decreasing trend, which is attributed to the BSA bilayer's ability to improve the stability of the Zn metal surface. In contrast, the impedances of the cell without BSA continuously increased upon cycling (Figure S21). Based on the EIS results, we calculated the ionic conductivity of the SEI according to the equation $\sigma = l/(RA)$.[45] After the addition of BSA, the ionic conductivity of the SEI significantly increased from 1.55×10^{-6} S cm^{-1} to 4.97×10^{-6} S cm^{-1}. This enhancement demonstrates that BSA effectively improves the ionic conductivity of the SEI layer, thereby enhancing the overall electrochemical performance of the Zn-ion batteries.

The cycling stability of the BSA-protected Zn anodes was first evaluated in Zn∥Zn symmetric cells. As shown in Figure 5d, the cell using the electrolyte with BSA exhibits a long cycle life of 2400 h at the current density of 10 mA cm^{-2} with the capacity limitation of 1 mAh cm^{-2}, which has surpassed most previous reported work (Figure S22 and Table S2). In contrast, the cell with pristine $ZnSO_4$ electrolyte exhibited a much shorter lifespan (700 h). The voltage profiles of the symmetric cells were compared at 0–3 h, 710– 713 h and 2400–2403 h (insets in Figure 5d). The voltage plateaus during both charging and discharging remained stable during cycling for the cell with the BSA additive, demonstrating dramatically enhanced cycling stability of Zn metal anodes. Additionally, the Zn∥Zn symmetric cells with BSA additive also exhibit excellent rate performance (Figure S23). The Coulombic efficiency (CE) of Zn plating/ stripping is crucial in assessing the cycling durability of Zn metal anodes as well.[46] Under the conditions of 2 mA cm^{-2} and 0.5 mAh cm^{-2}, the Zn∥Cu cell with the BSA additive in the electrolyte demonstrated stable cycling performance for over 4800 hours with an average Coulombic efficiency exceeding 99%, significantly outperforming the Zn∥Cu cell with the pristine electrolyte (Figure 5e). Comparative analysis of the voltage-specific capacity profiles shows that the Zn∥Cu cell with BSA additive maintained a high degree of congruence at different cycles (Figure 5f and 5g). Additionally, the SEM images in Figure S24 demonstrate that the BSA additive effectively suppresses the formation of Zn dendrites and promotes uniform Zn deposition. The CE tests prove that the BSA interfacial layer-protected Zn electrode sustains a highly reversible plating/stripping process throughout the long-term cycling up to 1000 cycles. To investigate the influence of the amount of the BSA additive in the electrolyte on the CEs of Zn metal anodes, Zn∥Cu
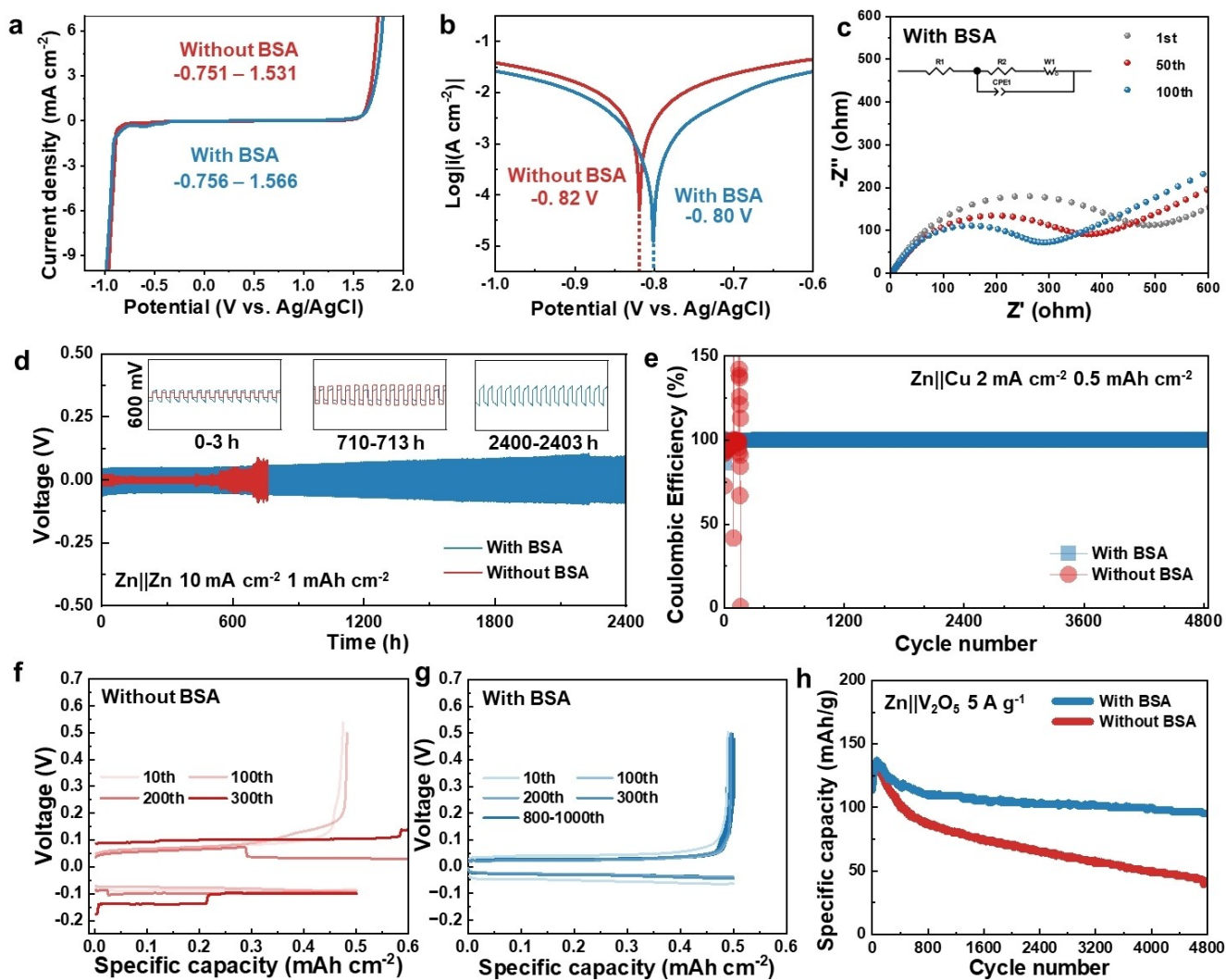
Figure 5. a) The electrochemical stability windows of the cells measured by LSV at 0.1 mV s^{-1}. b) Tafel plots of Zn anodes in aqueous electrolytes with and without BSA additive. c) The Nyquist plots of the assembled cell with BSA at different cycles. d) Cycling performance of Zn||Zn symmetric cells at a current density of 10 mA cm^{-2} with a capacity of 1 mAh cm^{-2}. e) The Coulombic efficiencies of Zn||Cu half cells using electrolytes with and without BSA at 2 mA cm^{-2} and 0.5 mAh cm^{-2}. f), g) The corresponding voltage vs. capacity profiles of the CE tests. h) The cycling performance of the assembled full cells with different electrolytes.

half cells were tested in the aqueous electrolytes with different concentrations of the BSA additive. As shown in Figure S25, the Zn||Cu half cells with the electrolyte containing 0.5 wt% BSA achieved the best cycling stability among other electrolytes. We believe that the high concentration of BSA (≥ 0.7 wt%) leads to chelation between Zn^{2+} ions and BSA functional groups, which reduces the conductivity of Zn^{2+} ions. Additionally, the excessive presence of BSA molecules may increase the thickness of the interfacial layer on the Zn anode, potentially blocking ion channels and increasing polarization.

We further investigate the cycling performances of Zn||V$_2$O$_5$ full cells using the electrolytes with and without the BSA additives. As shown in Figure 5h, at a high current density of 5 A g^{-1}, the capacities of the full cell with pristine electrolyte start to continuously decay after 60 cycles, indicating the deterioration of the Zn metal anode and the

depletion of aqueous electrolyte. In contrast, the full cell using the electrolyte with BSA maintained a high capacity over 4800 cycles, achieving a capacity retention rate of 94.69%. The significantly improved electrochemical performance of the cell with BSA additive demonstrates the excellent protecting capability of BSA interfacial toward Zn anodes in Zn||V$_2$O$_5$ full cells.

Conclusion

This study investigated BSA as an electrolyte additive to construct an interfacial layer on Zn metal anodes via a self-assembly process for dendrite-free Zn metal anodes. BSA molecules form a complex bilayer structure on the Zn anode, featuring a hydrophilic outer layer and a hydrophobic inner layer, which is crucial in optimizing Zn ion

migration and desolvation processes. The hydrophilic outer layer effectively reduces the activity of interfacial water molecules, while the hydrophobic inner layer blocks the intrusion of solvated water molecules, promoting the desolvation of $[Zn(H_2O)_6]^{2+}$ and reducing direct contact between water molecules and the Zn anode. This unique mechanism effectively suppresses the formation of Zn dendrites and significantly reduces the generation of by-products. Using Cryo-EM and XPS etching techniques, we successfully observed and confirmed the existence and detailed composition of the BSA bilayer on the Zn metal anode. In addition, the AIMD simulation and DFT calculation confirm that BSA can enhance the desolvation process of Zn^{2+} at the Zn anode by modifying the electrolyte's solvation structure, hence improving deposition efficiency by directing Zn^{2+} deposition on the Zn (002) plane. Electrochemical characterization results highlighted the significant contribution of the BSA bilayer in enhancing the cycling stability of Zn||Zn symmetric cells, Zn||Cu half-cells, and Zn||V_2O_5 full cells. Notably, the Zn||Zn battery demonstrated stable cycling performance for 2400 hours at a current density of $10\ mA\,cm^{-2}$ and a capacity limitation of $1\ mAh\,cm^{-2}$. Moreover, the Zn||V_2O_5 battery maintained a high specific capacity of $95\ mAh\,g^{-1}$ after 4800 cycles at a high current density of $5\ A\,g^{-1}$. This study opens a new avenue for developing safe, dendrite-free, high-energy density Zn metal anodes for Zn-ion batteries.

Supporting Information

The authors have cited additional references within the Supporting Information.[16,45,47–67]

Acknowledgements

Conflict of Interest

The authors declare no conflict of interest.

Data Availability Statement

The data that support the findings of this study are available from the corresponding author upon reasonable request.

[1] a) P. Xiong, Y. Kang, N. Yao, X. Chen, H. Mao, W.-S. Jang, D. M. Halat, Z.-H. Fu, M.-H. Jung, H. Y. Jeong, Y.-M. Kim, J. A. Reimer, Q. Zhang, H. S. Park, *ACS Energy Lett.* **2023**, *8*, 1613–1625; b) S. Chen, Y. Ying, L. Ma, D. Zhu, H. Huang, L. Song, C. Zhi, *Nat. Commun.* **2023**, *14*, 2925; c) L. Chen, *J. Solid State Electrochem.* **2024**, *28*, 507–515; d) B. Li, J. Quan, A. Loh, J. Chai, Y. Chen, C. Tan, X. Ge, T. S. Hor, Z. Liu, H. Zhang, Y. Zong, *Nano Lett.* **2017**, *17*, 156–163.

[2] a) C.-X. Zhao, X.-Y. Li, H. Han, Y. Feng, C. Tang, X. Li, L. Zhang, C. L. Stern, Q. Zhang, J. F. Stoddart, *Nat Chem Eng* **2024**, *1*, 251–260; b) Q. Yun, L. Li, Z. Hu, Q. Lu, B. Chen, H. Zhang, *Adv. Mater.* **2020**, *32*, 1903826; c) K. Chayambuka, G. Mulder, D. L. Danilov, P. H. Notten, *Adv. Energy Mater.* **2020**, *10*, 2001310; d) M. Jiang, D. L. Danilov, R. A. Eichel, P. H. Notten, *Adv. Energy Mater.* **2021**, *11*, 2103005.

[3] a) F. Wang, O. Borodin, T. Gao, X. Fan, W. Sun, F. Han, A. Faraone, J. A. Dura, K. Xu, C. Wang, *Nat. Mater.* **2018**, *17*, 543–549; b) L. E. Blanc, D. Kundu, L. F. Nazar, *Joule* **2020**, *4*, 771–799; c) N. Zhang, X. Chen, M. Yu, Z. Niu, F. Cheng, J. Chen, *Chem. Soc. Rev.* **2020**, *49*, 4203–4219.

[4] a) G. Liang, B. Liang, A. Chen, J. Zhu, Q. Li, Z. Huang, X. Li, Y. Wang, X. Wang, B. Xiong, X. Jin, S. Bai, J. Fan, C. Zhi, *Nat. Commun.* **2023**, *14*, 1856; b) X. Ge, W. Zhang, F. Song, B. Xie, J. Li, J. Wang, X. Wang, J. Zhao, G. Cui, *Adv. Funct. Mater.* **2022**, *32*, 2200429; c) T. Lv, G. Zhu, S. Dong, Q. Kong, Y. Peng, S. Jiang, G. Zhang, Z. Yang, S. Yang, X. Dong, H. Pang, Y. Zhang, *Angew. Chem. Int. Ed.* **2023**, *62*, e202216089.

[5] a) C. Yang, J. Xia, C. Cui, T. P. Pollard, J. Vatamanu, A. Faraone, J. A. Dura, M. Tyagi, A. Kattan, E. Thimsen, J. Xu, W. Song, E. Hu, X. Ji, S. Hou, X. Zhang, M. S. Ding, S. Hwang, D. Su, Y. Ren, X.-Q. Yang, H. Wang, O. Borodin, C. Wang, *Nat. Sustain.* **2023**, *6*, 325–335; b) R. Lv, H. Wu, Z. Jiang, A. Zheng, H. Yu, M. Chen, *Electrochim. Acta* **2022**, *429*, 140998.

[6] a) L. Cao, D. Li, T. Pollard, T. Deng, B. Zhang, C. Yang, L. Chen, J. Vatamanu, E. Hu, M. J. Hourwitz, L. Ma, M. Ding, Q. Li, S. Hou, K. Gaskell, J. T. Fourkas, X. Q. Yang, K. Xu, O. Borodin, C. Wang, *Nat. Nanotechnol.* **2021**, *16*, 902–910; b) H. Qiu, R. Hu, X. Du, Z. Chen, J. Zhao, G. Lu, M. Jiang, Q. Kong, Y. Yan, J. Du, X. Zhou, G. Cui, *Angew. Chem. Int. Ed.* **2022**, *61*, e202113086.

[7] a) Y. Li, L. Wu, C. Dong, X. Wang, Y. Dong, R. He, Z. Wu, *Energy Environ. Mater.* **2023**, *6*, e12423; b) X. Wang, C. Sun, Z. S. Wu, *SusMat* **2023**, *3*, 180–206; c) L. Xu, N. Xu, C. Yan, W. He, X. Wu, G. Diao, M. Chen, *J. Electroanal. Chem.* **2021**, *888*, 115196.

[8] a) J. Yang, R. Zhao, Y. Wang, Z. Hu, Y. Wang, A. Zhang, C. Wu, Y. Bai, *Adv. Funct. Mater.* **2023**, *33*, 2213510; b) S. Bai, Z. Huang, G. Liang, R. Yang, D. Liu, W. Wen, X. Jin, C. Zhi, X. Wang, *Adv. Sci.* **2024**, *11*, 2304549; c) X. Guo, G. He, *J. Mater. Chem. A* **2023**, *11*, 11987–12001.

[9] a) X. Lei, Z. Ma, L. Bai, L. Wang, Y. Ding, S. Song, A. Song, H. Dong, H. Tian, H. Tian, *Battery Energy* **2023**, *2*, 20230024; b) B. Zhou, B. Miao, Y. Gao, A. Yu, Z. Shao, *Small* **2023**, *19*, 2300895.

[10] a) H. Yan, S. Li, Y. Nan, S. Yang, B. Li, *Adv. Energy Mater.* **2021**, *11*, 2100186; b) R. Yuksel, O. Buyukcakir, W. K. Seong,

R. S. Ruoff, *Adv. Energy Mater.* **2020**, *10*, 1904215; c) J. Ren, C. Li, P. Li, S. Liu, L. Wang, *Chem. Eng. J.* **2023**, *462*, 142270.

[11] a) L. Hong, L. Y. Wang, Y. Wang, X. Wu, W. Huang, Y. Zhou, K. X. Wang, J. S. Chen, *Adv. Sci.* **2022**, *9*, 2104866; b) Y. Li, S. Yang, H. Du, Y. Liu, X. Wu, C. Yin, D. Wang, X. Wu, Z. He, X. Wu, *J. Mater. Chem. A* **2022**, *10*, 14399–14410; c) G. Fang, J. Zhou, A. Pan, S. Liang, *ACS Energy Lett.* **2018**, *3*, 2480–2501.

[12] X. Zeng, J. Mao, J. Hao, J. Liu, S. Liu, Z. Wang, Y. Wang, S. Zhang, T. Zheng, J. Liu, *Adv. Mater.* **2021**, *33*, 2007416.

[13] H. Yu, D. Chen, Q. Li, C. Yan, Z. Jiang, L. Zhou, W. Wei, J. Ma, X. Ji, Y. Chen, *Adv. Energy Mater.* **2023**, *13*, 2300550.

[14] C. Wang, C. Ying, J. Shang, S. E. Karcher, J. McCloy, J. Liu, W.-H. Zhong, *ACS Appl. Mater. Interfaces* **2022**, *14*, 43886–43896.

[15] a) J. Lu, J. Yang, Z. Zhang, C. Wang, J. Xu, T. Wang, *ChemSusChem* **2022**, *15*, e202200656; b) Q. Gou, H. Luo, Q. Zhang, J. Deng, R. Zhao, O. Odunmbaku, L. Wang, L. Li, Y. Zheng, J. Li, D. Chao, M. Li, *Small* **2023**, *19*, 2207502; c) T. Wang, D. He, H. Yao, X. Guo, B. Sun, G. Wang, *Adv. Energy Mater.* **2022**, *12*, 23; d) J. Xu, W. Lv, W. Yang, Y. Jin, Q. Jin, B. Sun, Z. Zhang, T. Wang, L. Zheng, X. Shi, B. Sun, G. Wang, *ACS Nano* **2022**, *16*, 11392–11404.

[16] C. Huang, J. Mao, S. Li, W. Zhang, X. Wang, Z. Shen, S. Zhang, J. Guo, Y. Xu, Y. Lu, J. Lu, *Adv. Funct. Mater.* **2024**, 2315855.

[17] Y. Wang, L. e. Mo, X. Zhang, Y. Ren, T. Wei, Z. Li, Y. Huang, H. Zhang, G. Cao, L. Hu, *Adv. Energy Mater.* **2023**, *13*, 2301517.

[18] a) T. Zhang, M. Tang, Y. Yao, Y. Ma, Y. Pu, *Int. J. Nanomed.* **2019**, *14*, 993–1009; b) H. Xu, N. Yao, H. Xu, T. Wang, G. Li, Z. Li, *Int. J. Mol. Sci.* **2013**, *14*, 14185–14203.

[19] X. Xu, J. Hu, H. Xue, Y. Hu, Y. N. Liu, G. Lin, L. Liu, R. A. Xu, *Int. J. Biol. Macromol.* **2023**, *253*, 126914.

[20] a) H. Shi, X. Ye, J. Zhang, T. Wu, T. Yu, C. Zhou, J. Ye, *Bioact. Mater.* **2021**, *6*, 1267–1282; b) A. M. Siddiq, D. Murugan, R. Srivastava, M. S. Alam, *Colloids Surf. B* **2019**, *184*, 110524.

[21] a) X. Chen, Y. Dai, Z. Huang, L. Zhao, J. Du, W. Li, D. Yu, *Ultrason. Sonochem.* **2022**, *89*, 106157; b) J. Lu, J. Yang, Z. Zhang, C. Wang, J. Xu, T. Wang, *ChemSusChem* **2022**, *15*, e202200656.

[22] a) J.-N. Longchamp, S. Rauschenbach, S. Abb, C. Escher, T. Latychevskaia, K. Kern, H.-W. Fink, *Proc. Natl. Acad. Sci. USA* **2017**, *114*, 1474–1479; b) M. J. Costello, *Ultrastruct. Pathol.* **2006**, *30*, 361–371.

[23] a) J. Zhang, J. Wen, W.-D. Liu, X. Cui, Y. Chen, *Sci. China Mater.* **2022**, *65*, 2613–2626; b) Y. Cui, L. Kourkoutis, *Acc. Chem. Res.* **2021**, *54*, 3619–3620.

[24] a) X. Wang, Y. Li, Y. S. Meng, *Joule* **2018**, *2*, 2225–2234; b) X. Wang, X. Li, H. Fan, L. Ma, *Nano-Micro Lett.* **2022**, *14*, 205.

[25] a) H. Fallatah, M. Elhaneid, H. Ali-Boucetta, T. W. Overton, H. El Kadri, K. Gkatzionis, *Environ. Sci. Pollut. Res. Int.* **2019**, *26*, 25057–25070; b) R. M. Firdaus, A. Desforges, M. Emo, A. R. Mohamed, B. Vigolo, *Nanomaterials* **2021**, *11*, 2419.

[26] H. Du, X. Li, P. Yao, J. Wang, Y. Sun, L. Dong, *Nanomaterials* **2018**, *8*, 509.

[27] a) C. Niu, J. Liu, T. Qian, X. Shen, J. Zhou, C. Yan, *Natl. Sci. Rev.* **2020**, *7*, 315–323; b) Q. Wen, H. Fu, Z.-y. Wang, Y.-d. Huang, Z.-j. He, C. Yan, J. Mao, K. Dai, X.-h. Zhang, J.-c. Zheng, *J. Mater. Chem. A* **2022**, *10*, 17501–17510.

[28] a) Y. Chen, Z. Yu, P. Rudnicki, H. Gong, Z. Huang, S. C. Kim, J.-C. Lai, X. Kong, J. Qin, Y. Cui, Z. Bao, *J. Am. Chem. Soc.* **2021**, *143*, 18703–18713; b) Z. Yu, P. E. Rudnicki, Z. Zhang, Z. Huang, H. Celik, S. T. Oyakhire, Y. Chen, X. Kong, S. C. Kim, X. Xiao, H. Wang, Y. Zheng, G. A. Kamat, M. S. Kim, S. F. Bent, J. Qin, Y. Cui, Z. Bao, *Nat. Energy* **2022**, *7*, 94–106.

[29] S. So, Y. N. Ahn, J. Ko, I. T. Kim, J. Hur, *Energy Storage Mater.* **2022**, *52*, 40–51.

[30] H. Liu, Y. Zhang, C. Wang, J. N. Glazer, Z. Shan, N. Liu, *ACS Appl. Mater. Interfaces* **2021**, *13*, 32930–32936.

[31] a) H. Zhang, Y. Zhong, J. Li, Y. Liao, J. Zeng, Y. Shen, L. Yuan, Z. Li, Y. Huang, *Adv. Energy Mater.* **2022**, *13*, 2203254; b) W. Yuan, X. Nie, Y. Wang, X. Li, G. Ma, Y. Wang, S. Shen, N. Zhang, *ACS Nano* **2023**, *17*, 23861–23871.

[32] a) J. Zhang, W. Huang, L. Li, C. Chang, K. Yang, L. Gao, X. Pu, *Adv. Mater.* **2023**, *35*, 2300073; b) Z. Zhao, R. Wang, C. Peng, W. Chen, T. Wu, B. Hu, W. Weng, Y. Yao, J. Zeng, Z. Chen, P. Liu, Y. Liu, G. Li, J. Guo, H. Lu, Z. Guo, *Nat. Commun.* **2021**, *12*, 6606.

[33] D. Wang, D. Lv, H. Peng, C. Wang, H. Liu, J. Yang, Y. Qian, *Angew. Chem. Int. Ed.* **2023**, *62*, e202310290.

[34] K. Liu, H. Gu, Y. Sun, C. Xu, S. Yang, B. Zhu, *Food Chem.* **2021**, *356*, 129658.

[35] A. Akhuli, D. Chakraborty, A. K. Agrawal, M. Sarkar, *Langmuir* **2021**, *37*, 1823–1837.

[36] a) X. Li, X. Wang, L. Ma, W. Huang, *Adv. Energy Mater.* **2022**, *12*, 2202068; b) H. Cheng, Q. Sun, L. Li, Y. Zou, Y. Wang, T. Cai, F. Zhao, G. Liu, Z. Ma, W. Wahyudi, Q. Li, J. Ming, *ACS Energy Lett.* **2022**, *7*, 490–513; c) T. Sun, X. L. Feng, Q. Q. Sun, Y. Yu, G. B. Yuan, Q. Xiong, D. P. Liu, X. B. Zhang, Y. Zhang, *Angew. Chem. Int. Ed.* **2021**, *60*, 26806–26812.

[37] a) L. Cao, D. Li, E. Hu, J. Xu, T. Deng, L. Ma, Y. Wang, X. Q. Yang, C. Wang, *J. Am. Chem. Soc.* **2020**, *142*, 21404–21409; b) H. Du, R. Zhao, Y. Yang, Z. Liu, L. Qie, Y. Huang, *Angew. Chem. Int. Ed.* **2022**, *61*, e202114789.

[38] M. S. Kim, Z. Zhang, J. Wang, S. T. Oyakhire, S. C. Kim, Z. Yu, Y. Chen, D. T. Boyle, Y. Ye, Z. Huang, W. Zhang, R. Xu, P. Sayavong, S. F. Bent, J. Qin, Z. Bao, Y. Cui, *ACS Nano* **2023**, *17*, 3168–3180.

[39] T. Wei, H. Zhang, Y. Ren, L. e. Mo, Y. He, P. Tan, Y. Huang, Z. Li, D. Zhu, L. Hu, *Adv. Funct. Mater.* **2023**, 2312506.

[40] Z. Huang, Z. Li, Y. Wang, J. Cong, X. Wu, X. Song, Y. Ma, H. Xiang, Y. Huang, *ACS Energy Lett.* **2022**, *8*, 372–380.

[41] H. Zhang, Y. Zhong, J. Li, Y. Liao, J. Zeng, Y. Shen, L. Yuan, Z. Li, Y. Huang, *Adv. Energy Mater.* **2023**, *13*, 2203254.

[42] T. Zhou, Y. Mu, L. Chen, D. Li, W. Liu, C. Yang, S. Zhang, Q. Wang, P. Jiang, G. Ge, H. Zhou, *Energy Storage Mater.* **2022**, *45*, 777–785.

[43] a) J. Zhang, D.-W. Wang, W. Lv, S. Zhang, Q. Liang, D. Zheng, F. Kang, Q.-H. Yang, *Energy Environ. Sci.* **2017**, *10*, 370–376; b) J.-G. Han, J. B. Lee, A. Cha, T. K. Lee, W. Cho, S. Chae, S. J. Kang, S. K. Kwak, J. Cho, S. Y. Hong, N.-S. Choi, *Energy Environ. Sci.* **2018**, *11*, 1552–1562.

[44] H. Yan, S. Li, J. Zhong, B. Li, *Nano-Micro Lett.* **2024**, *16*, 15.

[45] a) Z. Wang, F. Hu, G. Duan, K. Shibata, S. Koshizuka, *Nucl. Eng. Des.* **2019**, *341*, 390–405; b) X. Fu, L. Scudiero, W.-H. Zhong, *J. Mater. Chem. A* **2019**, *7*, 1835–1848.

[46] a) J. Xu, H. Li, Y. Jin, D. Zhou, B. Sun, M. Armand, G. Wang, *Adv. Mater.* **2024**, *36*, 2309726; b) S. Jin, J. Yin, X. Gao, A. Sharma, P. Chen, S. Hong, Q. Zhao, J. Zheng, Y. Deng, Y. L. Joo, L. A. Archer, *Nat. Commun.* **2022**, *13*, 2283.

[47] a) X. Liu, Y. Gong, Y. Sun, Z. Xu, Y. Wang, *Comput. Theor. Chem.* **2022**, *1215*, 113812; b) S. Maiti, M. T. Curnan, K. Maiti, S. Choung, J. W. Han, *Chem* **2023**, *9*, 3415–3460; c) N. Yao, X. Chen, Z. H. Fu, Q. Zhang, *Chem. Rev.* **2022**, *122*, 10970–11021; d) A. Y. S. Eng, C. B. Soni, Y. Lum, E. Khoo, Z. Yao, S. K. Vineeth, V. Kumar, J. Lu, C. S. Johnson, C. Wolverton, Z. W. Seh, *Sci. Adv.* **2022**, *8*, eabm2422.

[48] a) Y. Liu, M. Paskevicius, M. V. Sofianos, G. Parkinson, C.-Z. Li, *Carbon* **2021**, *172*, 454–462; b) J. Li, J. K. Park, R. B. Moore, L. A. Madsen, *Nat. Mater.* **2011**, *10*, 507–511.

[49] M. Zhang, X. Liu, J. Gu, H. Wang, H. Liu, Z. Shen, *Chin. Chem. Lett.* **2023**, *34*, 108471.

[50] L. Wang, B. Zhang, W. Zhou, Z. Zhao, X. Liu, R. Zhao, Z. Sun, H. Li, X. Wang, T. Zhang, H. Jin, W. Li, A. Elzatahry, Y. Hassan, H. J. Fan, D. Zhao, D. Chao, *J. Am. Chem. Soc.* **2024**, *146*, 6199–6208.

[51] Y. Ai, C. Yang, Z. Yin, T. Wang, T. Gai, J. Feng, K. Li, W. Zhang, Y. Li, F. Wang, D. Chao, Y. Wang, D. Zhao, W. Li, *J. Am. Chem. Soc.* **2024**, *146*, 15496–15505.

[52] Y. Wang, L. e. Mo, X. Zhang, Y. Ren, T. Wei, Z. Li, Y. Huang, H. Zhang, G. Cao, L. Hu, *Adv. Energy Mater.* **2023**, *13*, 2301517.

[53] H. Lu, X. Zhang, M. Luo, K. Cao, Y. Lu, B. B. Xu, H. Pan, K. Tao, Y. Jiang, *Adv. Funct. Mater.* **2021**, *31*, 2103514.

[54] B. Wang, R. Zheng, W. Yang, X. Han, C. Hou, Q. Zhang, Y. Li, K. Li, H. Wang, *Adv. Funct. Mater.* **2022**, *32*, 2112693.

[55] H. Dong, X. Hu, R. Liu, M. Ouyang, H. He, T. Wang, X. Gao, Y. Dai, W. Zhang, Y. Liu, Y. Zhou, D. J. L. Brett, I. P. Parkin, P. R. Shearing, G. He, *Angew. Chem. Int. Ed.* **2023**, *62*, e202311268.

[56] H. Li, Y. Ren, Y. Zhu, J. Tian, X. Sun, C. Sheng, P. He, S. Guo, H. Zhou, *Angew. Chem. Int. Ed.* **2023**, *62*, e202310143.

[57] M. Qiu, P. Sun, Y. Wang, L. Ma, C. Zhi, W. Mai, *Angew. Chem. Int. Ed.* **2022**, *61*, e202210979.

[58] D. Feng, Y. Jiao, P. Wu, *Angew. Chem. Int. Ed.* **2023**, *62*, e202314456.

[59] Z. Zhang, X. Yang, P. Li, Y. Wang, X. Zhao, J. Safaei, H. Tian, D. Zhou, B. Li, F. Kang, G. Wang, *Adv. Mater.* **2022**, *34*, 2206970.

[60] X. Cai, W. Tian, Z. Zhang, Y. Sun, L. Yang, H. Mu, C. Lian, H. Qiu, *Adv. Mater.* **2024**, *36*, 2307727.

[61] Q. Deng, S. You, W. Min, Y. Xu, W. Lin, J. Lu, C. Yang, *Adv. Mater.* **2024**, 2312924.

[62] Y. Jiao, F. Li, X. Jin, Q. Lei, L. Li, L. Wang, T. Ye, E. He, J. Wang, H. Chen, *Adv. Funct. Mater.* **2021**, *31*, 2107652.

[63] D. Xie, Z. W. Wang, Z. Y. Gu, W. Y. Diao, F. Y. Tao, C. Liu, H. Z. Sun, X. L. Wu, J. W. Wang, J. P. Zhang, *Adv. Funct. Mater.* **2022**, *32*, 2204066.

[64] X. Ni, J. Zhou, H. Ji, Y. Chen, H. Yu, Y. Zheng, T. Qian, M. Wang, L. Chen, C. Yan, *Adv. Funct. Mater.* **2023**, *33*, 2302293.

[65] X. Xu, S. Li, H. Yan, J. Du, S. Yang, B. Li, *Adv. Funct. Mater.* **2024**, *34*, 2308661.

[66] T. Wang, P. Wang, L. Pan, Z. He, L. Dai, L. Wang, S. Liu, S. C. Jun, B. Lu, S. Liang, *Adv. Energy Mater.* **2023**, *13*, 2203523.

[67] P. Zou, R. Zhang, L. Yao, J. Qin, K. Kisslinger, H. Zhuang, H. L. Xin, *Adv. Energy Mater.* **2021**, *11*, 2100982.